# Supplementary information for Observation of many-body Fock space dynamics in two dimensions

## CONTENTS



## 1. EXPERIMENTAL SETUP

As shown in Fig. 1**a** of the main text, our experiment is carried out on a two-dimensional (2D) flip-chip superconducting quantum processor, which integrates 36 transmon qubits and 60 tunable couplers [1]. The former form a $6 \times 6$ square lattice, and the latter provide the nearest-neighbor connectivity. A diagrammatic sketch of on-chip control circuits for two qubits and a coupler is shown in the gray box of Fig. S1. Each qubit owns an individual control line, which enables the microwave (XY) control for the single-qubit rotation and the flux (Z) control for modulating its frequency. Meanwhile, each qubit is capacitively coupled to a readout resonator for its state discrimination. Similarly, each coupler owns an individual flux control line for tuning frequency. In this way, the coupling strength between the two connected qubits by the coupler can be effectively tuned as needed.

The experimental setup for the control and the measurement of this multi-qubit device is shown in Fig. S1. The device is loaded inside a dilution refrigerator (DR) with a base temperature of $\sim 20$ mK. The control pulses, such as XY pulses, fast (slow) Z pulses, and microwave readout pulses are generated by room-temperature electronics (dashed box in Fig. S1), which are transmitted to the device after a series of attenuating, filtering at different cold stages in the DR. The digital to analog converter (DAC) channels are used individually for the fast Z controls of qubits and couplers, and in pairs for generating XY control pulses or readout pulses via frequency mixing with local oscillator signals. In addition, there is a low-noise slow Z (DC) control channel for biasing qubit to its idle frequency. For the frequency-multiplexed qubit readout, every nine qubits share a common readout transmission line, and the output readout signals from the device are amplified sequentially by a Josephson parametric amplifier (JPA) at the mixing chamber and a high electron mobility transistor (HEMT) amplifier at the 3K stage. At room temperature, readout signals are further amplified by room-temperature amplifiers and mixed down via the IQ mixer module. Finally, qubit state information is extracted with a demodulation process on analog-to-digital converters (ADCs).

## 2. DEVICE PERFORMANCE

The device is fabricated using the flip-chip recipe (see Ref. [2] for more fabrication details). In current experiment, we utilize up to 24 ($4 \times 6$) qubits and 38 couplers, but we collect the performance for all 36 qubits in Table S1. It is outstanding that the average energy relaxation time $T_1$ is more than 120 $\mu$s in our device. In addition, the dephasing time measured with spin echo (Hahn echo) experiment is $\sim$23 $\mu$s. Both of them are much longer than the maximum evolution time ($t_{\max}$ =1000 ns) in our experiment, and thus make it possible to observe the coherent quantum many-body dynamics before decoherence effects are substantial. Average single-qubit gate fidelities measured by simultaneous randomized benchmarking are $\sim 0.9968$ for 36 qubits (see Table S1), and $\sim 0.9978$ for the 24 qubits used in our experiment.

## 3. EXPERIMENTAL CALIBRATIONS

We use quench protocol to investigate many-body dynamics. As shown in Fig. S2, the experimental sequence includes three steps: state preparation, interaction and measurement. For the initial state preparation, all qubits and couplers stay at their idle points, where half of qubits are excited to $|1\rangle$ states by $\pi$ pulses (orange Gaussian-shape waveforms). Then, all qubits are suddenly tuned to their interaction frequencies via fast Z pulses. At the same time, all couplers are biased for realizing target cou-

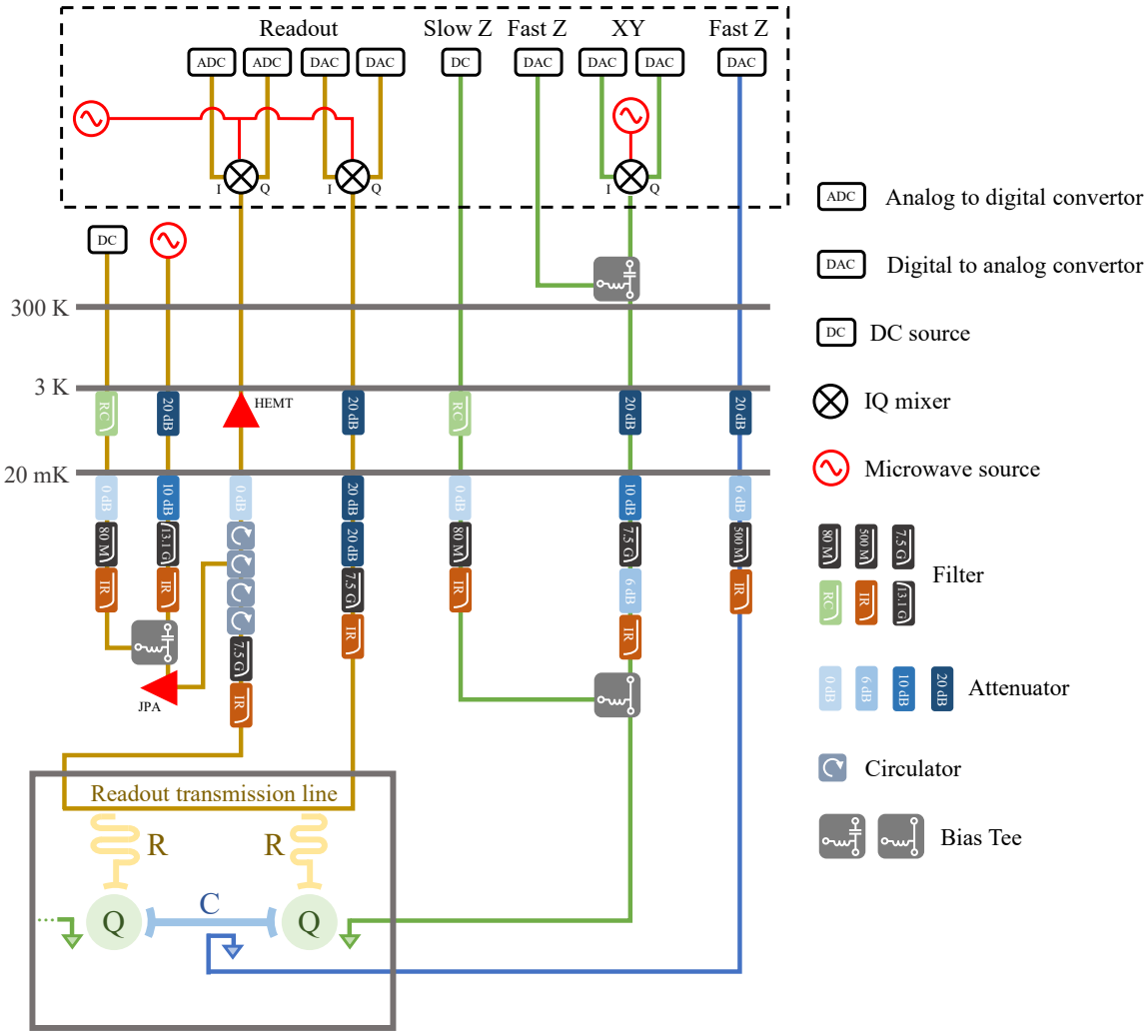


FIG. S1. **Experimental setup.** The cartoon diagram schematically shows the connection of room-temperature electronics (DACs, ADCs, and IQ mixers) and cryogenic wirings (cables, attenuators, filters, circulators, and amplifiers) for controlling and measuring our device. The layout in the left-lower gray box represents the device, where Q, C, and R indicate the qubit, coupler, and readout resonator, respectively. Different stages of DR, including mixing chamber (20 mK), 3 K plate and 300 K plate are indicated by horizontal thick gray lines, where attenuators, filters, circulators and amplifiers are mounted. The top dashed rectangular box illustrates the room-temperature electronics for generating control signals and demodulating readout signals.

pling strengths in the same way. After an evolution time $t$, all couplers are tuned back to idle points and all qubits are tuned to their respective readout frequencies for state measurements.

In our experiment, fast Z pulses play a substantial role in tuning frequencies (disorder strength), which makes their calibrations more important. Here, we take qubit $Q_{(4,6)}$ as an example to show its calibrations. To minimize the crosstalk effect on final multi-qubit experiments, we keep all other qubits stay near the interaction frequency $\omega_I$ and all couplers stay on target coupling strength when we use spectroscopy experiment to map the relationship between qubit frequency and Z pulse amplitude. The measured spectroscopy data is shown in Fig. S3**a**. There are two branches above and below $\omega_I$ due to the avoided crossing. With a polynomial fitting of these two branches (see Fig. S3**b**), we could extract a function of Z pulse amplitude versus qubit frequency ranging from 4.4 GHz to 4.7 GHz.

## 4. EFFECTIVE HAMILTONIAN

Equation (1) in the main text is the effective Hamiltonian of our model and its tunable interactions between nearest-neighbor (NN) qubit pairs is enabled by the adjacent couplers. Here, we show the derivation of effective Hamiltonian from its original configurations including couplers. At first, the full Hamiltonian ($\hbar = 1$) in a

| Qubit Index | $\omega_{(m,n)}/2\pi$ (GHz) | $T_{1,(m,n)}^{(\mathrm{idle})}$ ($\mu$s) | $T_{1,(m,n)}^{(\mathrm{inte.})}$ ($\mu$s) | $T_{2,(m,n)}^{*}$ ($\mu$s) | $T_{2,(m,n)}^{SE}$ ($\mu$s) | $F_{0,(m,n)}$ | $F_{1,(m,n)}$ | $e_{\mathrm{sq}}$ (%) |
|---|---|---|---|---|---|---|---|---|
| $Q_{(1,1)}$ | 4.630 | ∼169 | ∼147 | ∼3.6 | ∼10.7 | 0.973 | 0.950 | 0.20 |
| $Q_{(1,2)}$ | 4.780 | ∼117 | ∼114 | ∼8.8 | ∼27.3 | 0.988 | 0.962 | 0.40 |
| $Q_{(1,3)}$ | 4.881 | ∼130 | ∼119 | ∼7.0 | ∼19.8 | 0.979 | 0.946 | 0.53 |
| $Q_{(1,4)}$ | 4.704 | ∼132 | ∼132 | ∼3.9 | ∼13.3 | 0.976 | 0.946 | 0.58 |
| $Q_{(1,5)}$ | 4.597 | ∼96 | ∼100 | ∼4.7 | ∼21.4 | 0.974 | 0.893 | 0.17 |
| $Q_{(1,6)}$ | 4.509 | ∼150 | ∼114 | ∼5.2 | ∼20.0 | 0.970 | 0.915 | 0.14 |
| $Q_{(2,1)}$ | 4.368 | ∼160 | ∼117 | ∼5.0 | ∼21.6 | 0.967 | 0.923 | 0.27 |
| $Q_{(2,2)}$ | 4.826 | ∼163 | ∼90 | ∼2.8 | ∼9.45 | 0.975 | 0.928 | 0.22 |
| $Q_{(2,3)}$ | 4.752 | ∼132 | ∼87 | ∼6.2 | ∼21.7 | 0.986 | 0.952 | 0.13 |
| $Q_{(2,4)}$ | 4.679 | ∼132 | ∼118 | ∼3.8 | ∼13.8 | 0.979 | 0.899 | 0.33 |
| $Q_{(2,5)}$ | 4.643 | ∼138 | ∼128 | ∼3.0 | ∼13.4 | 0.976 | 0.926 | 0.22 |
| $Q_{(2,6)}$ | 4.471 | ∼108 | ∼139 | ∼10.6 | ∼36.9 | 0.972 | 0.912 | 0.20 |
| $Q_{(3,1)}$ | 4.542 | ∼119 | ∼150 | ∼7.3 | ∼30.9 | 0.978 | 0.888 | 0.15 |
| $Q_{(3,2)}$ | 4.791 | ∼142 | ∼120 | ∼6.0 | ∼20.7 | 0.953 | 0.947 | 0.33 |
| $Q_{(3,3)}$ | 4.615 | ∼110 | ∼136 | ∼3.6 | ∼10.4 | 0.966 | 0.898 | 0.28 |
| $Q_{(3,4)}$ | 4.722 | ∼133 | ∼157 | ∼8.7 | ∼28.7 | 0.989 | 0.970 | 0.35 |
| $Q_{(3,5)}$ | 4.666 | ∼139 | ∼160 | ∼4.0 | ∼14.1 | 0.982 | 0.954 | 0.59 |
| $Q_{(3,6)}$ | 4.492 | ∼106 | ∼130 | ∼9.0 | ∼33.7 | 0.969 | 0.863 | 0.45 |
| $Q_{(4,1)}$ | 4.387 | ∼141 | ∼114 | ∼7.5 | ∼20.7 | 0.974 | 0.936 | 0.24 |
| $Q_{(4,2)}$ | 4.432 | ∼155 | ∼152 | ∼6.6 | ∼19.4 | 0.969 | 0.949 | 0.38 |
| $Q_{(4,3)}$ | 4.522 | ∼152 | ∼132 | ∼5.2 | ∼15.0 | 0.981 | 0.942 | 0.28 |
| $Q_{(4,4)}$ | 4.761 | ∼157 | ∼127 | ∼7.3 | ∼24.7 | 0.987 | 0.942 | 0.13 |
| $Q_{(4,5)}$ | 4.803 | ∼154 | ∼112 | ∼6.3 | ∼23.5 | 0.990 | 0.948 | 0.12 |
| $Q_{(4,6)}$ | 4.560 | ∼121 | ∼118 | ∼5.3 | ∼21.1 | 0.988 | 0.952 | 0.16 |
| $Q_{(5,1)}$ | 4.813 | ∼114 | ∼133 | ∼8.8 | ∼17.5 | 0.917 | 0.873 | 0.40 |
| $Q_{(5,2)}$ | 4.652 | ∼127 | ∼120 | ∼7.6 | ∼23.5 | 0.957 | 0.872 | 0.42 |
| $Q_{(5,3)}$ | 4.686 | ∼89 | ∼120 | ∼7.4 | ∼31.9 | 0.942 | 0.862 | 0.29 |
| $Q_{(5,4)}$ | 4.715 | ∼103 | ∼89 | ∼14.1 | ∼58.0 | 0.953 | 0.916 | 0.73 |
| $Q_{(5,5)}$ | 4.604 | ∼104 | ∼99 | ∼5.8 | ∼18.1 | 0.974 | 0.886 | 0.36 |
| $Q_{(5,6)}$ | 4.751 | ∼131 | ∼102 | ∼10.5 | ∼42.1 | 0.972 | 0.947 | 0.28 |
| $Q_{(6,1)}$ | 4.764 | ∼151 | ∼150 | ∼6.4 | ∼19.8 | 0.988 | 0.944 | 0.73 |
| $Q_{(6,2)}$ | 4.403 | ∼118 | ∼102 | ∼3.1 | ∼9.7 | 0.921 | 0.886 | 0.23 |
| $Q_{(6,3)}$ | 4.462 | ∼115 | ∼155 | ∼4.9 | ∼15.5 | 0.960 | 0.900 | 0.26 |
| $Q_{(6,4)}$ | 4.838 | ∼127 | ∼129 | ∼8.3 | ∼35.1 | 0.973 | 0.924 | 0.17 |
| $Q_{(6,5)}$ | 4.806 | ∼116 | ∼129 | ∼9.4 | ∼30.5 | 0.969 | 0.944 | 0.62 |
| $Q_{(6,6)}$ | 4.858 | ∼121 | ∼101 | ∼7.6 | ∼37.2 | 0.963 | 0.938 | 0.22 |
| mean | 4.652 | ∼130 | ∼123 | ∼6.5 | ∼23.1 | 0.970 | 0.925 | 0.32 |

TABLE S1. **Device performance.** $\omega_{(m,n)}$ is the idle frequency of $Q_{(m,n)}$ where single-qubit XY pulses are applied for preparing initial Fock states. $T_{1,(m,n)}^{(\mathrm{idle})}$ and $T_{1,(m,n)}^{(\mathrm{inte.})}$ are the energy relaxation times of $Q_{(m,n)}$ measured at its idle frequency $\omega_{(m,n)}$ and the interaction frequency ($\omega_I/2\pi \approx 4.57$ GHz), respectively. $T_{2,(m,n)}^{*}$ and $T_{2,(m,n)}^{SE}$ are the ramsey and spin echo dephasing times of $Q_{(m,n)}$ measured at $\omega_{(m,n)}$. The readout fidelities are characterized by the measured probability when $Q_{(m,n)}$ is prepared in state $|0\rangle$ ($|1\rangle$), labeled by $F_{0,(m,n)}$ ($F_{1,(m,n)}$). Single-qubit gate errors $e_{\mathrm{sq}}$ are measured with randomized benchmarking (RB) on 36 qubits simultaneously. We note that such average $e_{\mathrm{sq}}$ is about 0.22% for the simultaneous RB on the 24 actively used qubits in the experiment.

general configuration is written as

$$\begin{aligned} H_0 = &\sum_m \omega_m \sigma_m^+ \sigma_m^- + \sum_j \omega_j \tau_j^+ \tau_j^- \\ &+ \sum_{m,j} g_{mj}(\sigma_m^+ \tau_j^- + \sigma_m^- \tau_j^+) \\ &+ \sum_{m,n} g_{mn}(\sigma_m^+ \sigma_n^- + \sigma_m^- \sigma_n^+), \end{aligned} \tag{S1}$$

where $g_{mn}$ ($g_{mj}$) is the coupling strength between qubit $Q_m$ and qubit $Q_n$ (qubit $Q_m$ and coupler $C_j$), $\sigma_m^{\pm}$ and $\tau_j^{\pm}$ are the raising (lowering) operators for qubit $Q_m$ and coupler $C_j$, respectively. The long-range couplings are very small, thus, we only consider the qubit-qubit couplings for the qubit pairs separated with the distance $R_{mn} = |\mathbf{r}_m - \mathbf{r}_n| \leq \sqrt{2}a_0$, where $a_0$ is the lattice constant of 2D qubit lattice and $\mathbf{r}_m$, $\mathbf{r}_n$ are the positions of $Q_m$ and $Q_n$, respectively.

In the regime of $g_{mj}$ ($g_{nj}$) $> g_{mn} > 0$, $\Delta_{m(n)} = \omega_{m(n)} - \omega_j < 0$, and $g_{m(n)j} \ll |\Delta_{m(n)}|$, such a Hamiltonian can be applied with the Schrieffer-Wolff transformation [3]

$$U = \sum_{R_{mn}=a_0} e^{\frac{g_{mj}}{\Delta_m}(\sigma_m^+ \tau_j^- - \sigma_m^- \tau_j^+) + \frac{g_{nj}}{\Delta_n}(\sigma_n^+ \tau_j^- - \sigma_n^- \tau_j^+)} \tag{S2}$$

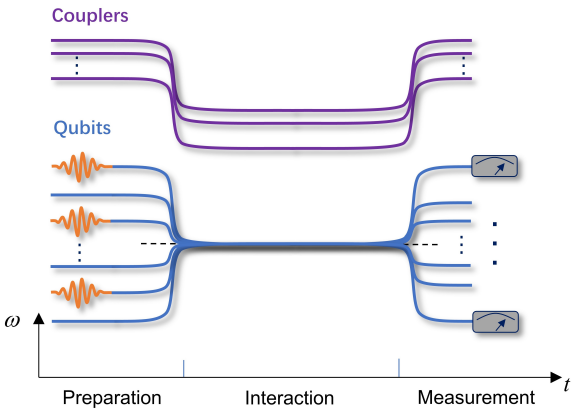


FIG. S2. **Pulse sequence.** There are three steps (preparation, interaction and measurement) for the experimental pulse sequence. $\omega$ axis indicates the frequency domain of qubits and couplers. The $\pi$ pulses for exciting qubits are denoted by orange Gaussian-shape envelopes. The black dashed line represents the interaction frequency $\omega_I/2\pi = 4.57$ GHz where qubits interact with each other when disorders are absent.

to the first order of $g_{m(n)j}/\Delta_{m(n)}$. Then, we have the transformed Hamiltonian as

$$H = \sum_m \omega'_m \sigma_m^+ \sigma_m^- + \sum_{m,n} J_{mn}(\sigma_m^+ \sigma_n^- + \text{h.c.}), \tag{S3}$$

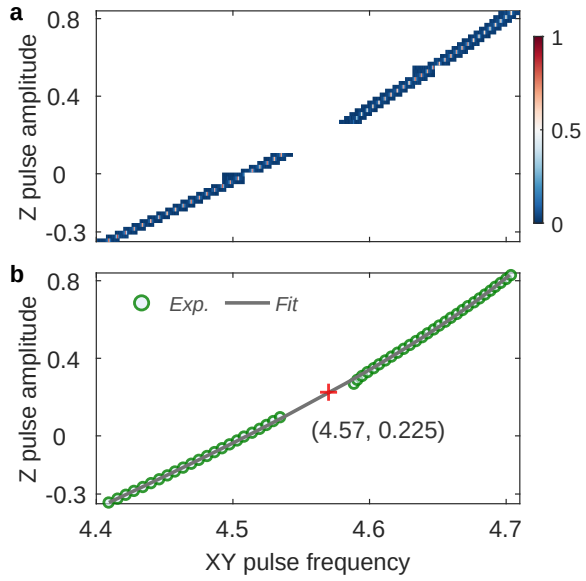


FIG. S3. **Frequency calibrations: Z pulse amplitude versus qubit frequency.** **a**, The raw data of the spectroscopy measurements for qubit $Q_{(4,6)}$ when all other qubits are tuned to $\omega_I$ and all the couplers are tuned to the target coupling configuration for many-body interactions. **b**, The polynomial fitting (gray line) for the experimental spectroscopy data (green circles) extracted from **a**.

with

$$\begin{aligned} \omega'_m &= \omega_m + \frac{g_{mj}^2}{\Delta_m}, \\ J_{mn} &= \frac{g_{mj} g_{nj}}{\Delta} + g_{mn}, \\ \frac{2}{\Delta} &= \frac{1}{\Delta_{mj}} + \frac{1}{\Delta_{nj}}. \end{aligned} \tag{S4}$$

In the rotating frame of $\omega_I$, we can get the effective Hamiltonian in real space as

$$H_{\text{R}} = \sum_m V_m \sigma_m^+ \sigma_m^- + \sum_{m,n} J_{mn}(\sigma_m^+ \sigma_n^- + \text{h.c.}), \tag{S5}$$

where $V_m = \omega'_m - \omega_I$. Equation (1) of the main text is just the 2D form of Equation (S5) and $J_{mn}$ includes all the NN couplings ($\chi_m$, $\gamma_n$) and cross couplings ($g_x$).

In order to realize a 2D SSH model with many-body scarring, we set $J_o/2\pi = 2J_e/2\pi = -6$ MHz and $g_{\text{x}}/2\pi = 0.9$ MHz in our model, which are used for the numerical simulations. Effective coupling strengths $\{J_{mn}\}$ measured by two-qubit photon swapping experiments at $\omega_I/2\pi = 4.57$ GHz are illustrated in Fig. S4 for NN couplings and Fig. S5 for cross couplings. We choose $V_m$ from a uniform random distribution $[-V, V]$ to mimic a fully disordered system. $V_m$ can be tuned individually by adjusting $Q_m$'s frequency without noticeably altering $\{J_{mn}\}$.

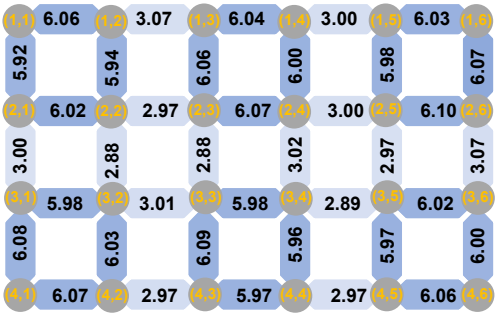


FIG. S4. **Experimentally measured nearest-neighbor couplings**. Gray circles represent qubits, and the chamfered rectangles connecting them denote the nearest-neighbor couplings with values for $-J_{mn}/2\pi$ (MHz) listed.

## 5. MECHANISM OF 2D MANY-BODY SCARRING

Inspired by the scarring phenomenon in the 1D XY model [4], here, we consider a 2D SSH lattice constructed by a set of tetramers. The intra- and inter-tetramer couplings are denoted by $J_{\text{o}}$ and $J_{\text{e}}$, respectively. To understand the scarring phenomenon, we begin to focus on a single tetramer with a square geometry that includes

four qubits. In the half-filling condition, a special kind of entangled eigenstates is given by

$$|E_{\rm sp}\rangle = \frac{1}{\sqrt{2}}\left[\left|\begin{matrix}\bullet & \circ\\ \circ & \bullet\end{matrix}\right\rangle - \left|\begin{matrix}\circ & \bullet\\ \bullet & \circ\end{matrix}\right\rangle\right], \tag{S6}$$

where $|\circ\rangle$ and $|\bullet\rangle$ represent the ground and excited states of a qubit, respectively. Then, when such tetramers are connected with a weak coupling $J_{\rm e}$, a pair of special Fock product states, $|\mathbf{s}_0^S\rangle$ and $|\mathbf{s}_0^{S\prime}\rangle$, partially inherit properties from the single tetramer. Thus, for a half-filling $4\times 6$ system, a scarred initial product state is given by

$$|\mathbf{s}_0^S\rangle = \left|\begin{matrix}\bullet & \circ\\ \circ & \bullet\end{matrix}\right| \left|\begin{matrix}\circ & \bullet\\ \bullet & \circ\end{matrix}\right| \left|\begin{matrix}\bullet & \circ\\ \circ & \bullet\end{matrix}\right| \left|\begin{matrix}\circ & \bullet\\ \bullet & \circ\end{matrix}\right| \left|\begin{matrix}\bullet & \circ\\ \circ & \bullet\end{matrix}\right| \left|\begin{matrix}\circ & \bullet\\ \bullet & \circ\end{matrix}\right|, \tag{S7}$$

where the block marks a tetramer. Each tetramer has a $\pi$-phase difference from its adjacent ones. As a system has the particle-hole symmetry, the Fock product state $|\mathbf{s}_0^{S\prime}\rangle$ has the same properties with the inverse state for each qubit.

Product states $|\mathbf{s}_0^S\rangle$ and $|\mathbf{s}_0^{S\prime}\rangle$ have remarkable overlap with a set of special eigenstates, which are equally spaced in the energy spectrum. The numerical simulation of energy level-spacing distribution for $4\times 4$ lattice agrees with the Wigner-Dyson type, as shown in Fig. S6. If we prepare the initial state as $|\mathbf{s}_0^S\rangle$ or $|\mathbf{s}_0^{S\prime}\rangle$, their fidelity dynamics show revival behaviors, and the dynamics of bipartite entanglement entropy (EE) also shows a slower growth.

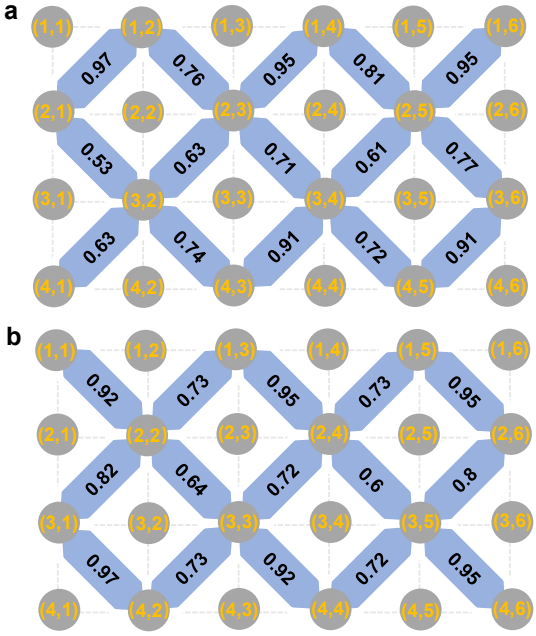


FIG. S5. **Experimentally measured cross couplings.** Gray circles represent qubits, and the chamfered rectangles connecting them denote the measured cross couplings with their values listed (MHz).

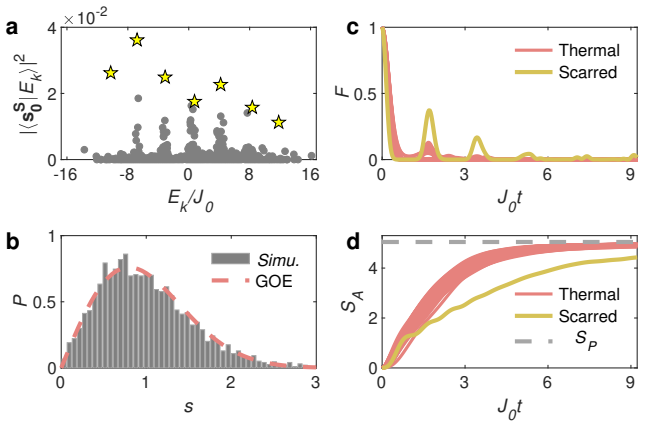


FIG. S6. **Properties of 2D scar.** Panel **a** shows the overlap between the scarred state $|\mathbf{s}_0^S\rangle$ and all eigenstates as a function of eigenenergy $E_k$. Yellow pentagrams mark the towers' peaks, representing a set of special scarred eigenstates. Panel **b** shows the level spacing distribution in a particle-hole symmetry sector. Compared to the GOE curve, this simulation result implies the absence of integrability. Panels **c** and **d** show the dynamics of fidelity and bipartite EE, respectively, for different initial product states. Red curves represent 20 randomly chosen thermal states, while yellow one represents the scarred state. Gray dashed line in **d** is the Page value of bipartite EE, $S_P$. Both **c** and **d** show that the scarred state has a slow thermalizing behavior. All simulation results are based on a disorder-free 2D SSH model in $4\times 4$ lattice with couplings $J_{\rm o}/2\pi = 2J_{\rm e}/2\pi = -6$ MHz and $g_{\rm x}/2\pi = 0.9$ MHz.

On the contrary, other product states show a thermalizing behavior, implied by their fidelity and bipartite EE dynamics, in which their initial information ergodically disperses in the whole Hilbert space.

## 6. LOCAL OBSERVABLES IN REAL SPACE

In general, measuring local observables in real space is the conventional way to study the quantum many-body dynamics experimentally. The population dynamics $p_m(t)$ for each qubit in real space help us to identify many-body states. As shown in Fig. S7 and Fig. S8, the population dynamics for both experimental data and numerical data are in good agreement with each other. For the scarred initial state $|\mathbf{s}_0^S\rangle$, the populations show remarkable oscillating patterns (Fig. S7**a**, **b**). In contrast, populations for all the qubits rapidly approach to a stable value of 0.5 for the thermal initial state $|\mathbf{s}_0^T\rangle$ (Fig. S7**c**, **d**). In the presence of disorders, the dynamics can preserve the initial populations for a long time, as shown in Fig. S8. In addition to the population dynamics, a quantity known as the generalized imbalance $I(t)$ [5] is also commonly used to describe the preservation of initial

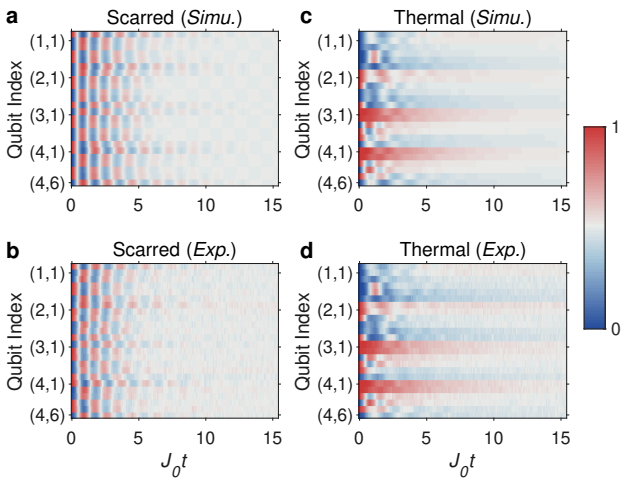


FIG. S7. **Population dynamics without disorder.** Panels **a** and **b** show the numerical and experimental population dynamics for the scarred state $|\mathbf{s}_0^S\rangle$, respectively. Panels **c** and **d** show similar results for the thermal state $|\mathbf{s}_0^T\rangle$.

local information in real space. Its definition is given by

$$I(t) = \frac{1}{L}\sum_{m=1}^{L}\langle\sigma_m^z(t)\rangle\langle\sigma_m^z(0)\rangle, \tag{S8}$$

where $\langle\sigma_m^z(t)\rangle = 2p_m(t) - 1$. We note that initial states are prepared as Fock states in the half-filling condition and $I(t=0) = 1$. As expected, the scarred dynamics exhibits strong oscillations and remain for a considerable period of time [6] (Fig. S9**a**), while the thermalizing dynamics quickly drop to zero (Fig. S9**b**). For the disordered system, the imbalance tends to stabilize at a finite value much larger than zero (Fig. S9**c** and **d**).

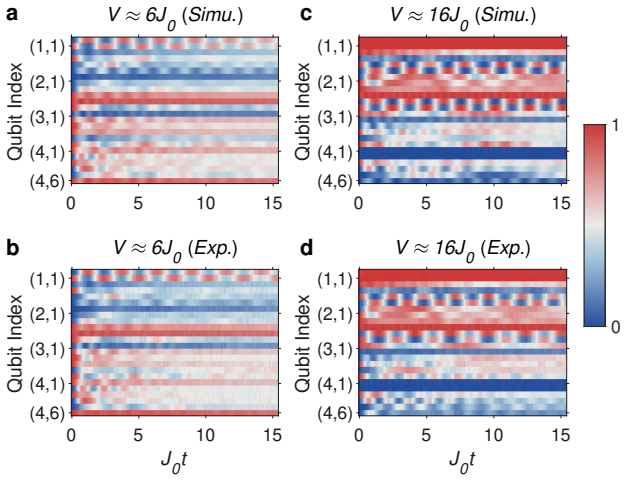


FIG. S8. **Population dynamics with disorder.** Panels **a** and **b** show the numerical and experimental population dynamics for $V \approx 6J_0$, respectively. Panels **c** and **d** are the similar results for a much larger disorder strength $V \approx 16J_0$.

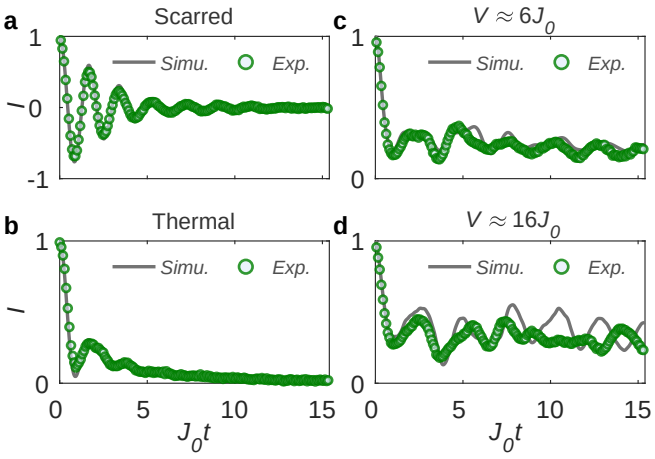


FIG. S9. **Imbalance dynamics.** Panels **a** and **b** show imbalance $I(t)$ for the scarred state $|\mathbf{s}_0^S\rangle$ and the thermal state $|\mathbf{s}_0^T\rangle$ at $V = 0$, respectively. Panels **c** and **d** show the $I(t)$ in disordered systems with $V \approx 6J_0$ and $16J_0$, respectively. Green circle markers represent the experiment data, and gray lines represent the numerical data.

## 7. FEW-BODY ENTANGLEMENT ENTROPY

For a quantum many-body system with a system size of $L$, it can be decomposed into two subsystems A and B in real space, with subsystem size $l_A$ and $l_B = L - l_A$. The reduced density matrix of subsystem A is given by $\rho_A = \mathrm{tr}_B(\rho)$, where $\rho$ is the density matrix for the whole system. Then, the von Neumann entanglement entropy is given by

$$S_A = -\mathrm{tr}\left(\rho_A \log \rho_A\right), \tag{S9}$$

which depicts the entanglement complexity between two subsystems.

The experimentally measured four-qubit ($l_A = 4$) EE are shown in Fig. S10 for the scarred, thermal, and localized states. For the scarred state, the growth of EE is slower than the thermalizing dynamics but eventually reaches the similar thermal value. In the presence of disorder ($V \approx 16J_0$), the EE grows slowly and tends to saturate to a value much smaller than thermal value, indicating the many-body localization in our finite-sized system.

## 8. LIMITATION OF FEW-BODY OBSERVABLES

Even though few-body EE is experimentally measurable, compared to global quantities (e.g., bipartite EE), it may fail to characterize the entanglement information of the whole system precisely [7]. Fig. S11 displays numerical results of EE with different subsystem size $l_A$ for $4\times4$ square lattice. Obviously, the bipartite ($l_A = L/2$) EE shows the sharpest transition peak from thermalization to localization. On the contrary, the standard deviation

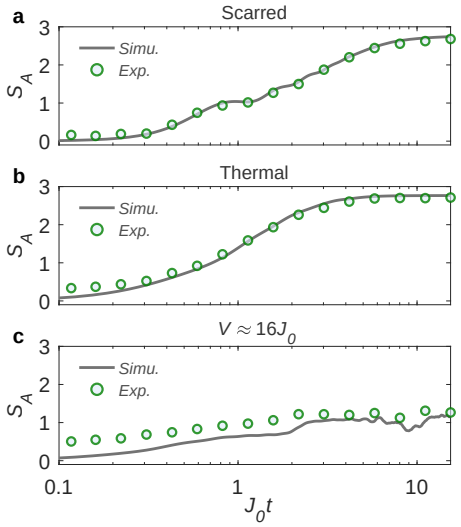


FIG. S10. **Time evolution of four-qubit entanglement entropy.** Four-qubit EE as a function of evolution time in log scale are shown in panel **a** for the scarred state $|\mathbf{s}_0^S\rangle$ ($V = 0$), panel **b** for the thermal state $|\mathbf{s}_0^T\rangle$ ($V = 0$), and panel **c** for the nonergodic dynamics of $V \approx 16J_0$. Gray lines represent the simulation results, while green circles represent the experiment data.

of two-qubit EE totally misses the transition point, and the four-qubit case shows a broad range of indistinctive enhancement of $\Delta S$, leading to an inaccurate estimation of critical disorder strength. Despite the reliability of bipartite EE, it is exponentially hard for numerics and experiments with the growth of system size, which makes its scaling analysis impossible for large systems.

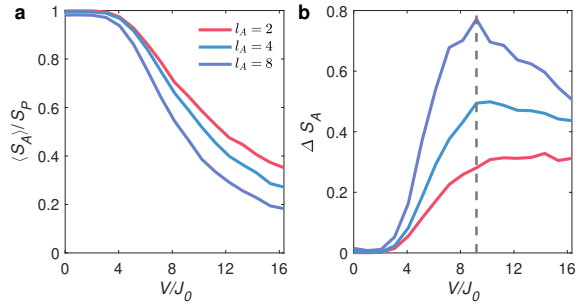


FIG. S11. **Numerical entanglement entropy for different subsystem sizes.** Panel **a** and **b** show the disorder-averaged ($k = 800$) subsystem entanglement entropy $\langle S_A \rangle$ and its standard deviation $\Delta S_A$ for $4\times4$ SSH model ($J_o/2\pi = 2J_e/2\pi = -6$ MHz, $g_x/2\pi = 0.9$ MHz) at $t = 1000$ ns, respectively. $l_A$ represents the site number of the subsystem $A$. Compared with few-body results ($l_A$ =2, 4), the bipartite EE ($l_A = L/2 = 8$) is much more efficient in depicting the critical behavior of the MBL transition. The estimated critical disorder with bipartite EE is marked by the gray dashed line.

## 9. SELECTION OF INITIAL STATES

Fock product states $|\mathbf{s}\rangle$ are friendly to prepare for experiments. However, after long-time evolution, not all of them have similar properties to the eigenstates of the middle spectrum due to the possible existence of many-body mobility edges [5, 8]. In our work, we choose the Fock product states in the center of the energy spectrum. The energy of each Fock state can be obtained easily by $E/\hbar = \sum_{m,Q_m=|1\rangle} V_m$. Since the energy spectrum of the Hamiltonian for larger systems is approximately Gaussian distributed, we can approximate the energy in the middle by numerically averaging the maximum and minimum eigenvalues ($E_{\rm mid} = (E_{\rm max} + E_{\rm min})/2$). Thus, we randomly select one Fock state with energy $E$ in the range of $[E_{\rm mid} - \Delta E/100, E_{\rm mid} + \Delta E/100]$ for each realization, where $\Delta E = E_{\rm max} - E_{\rm min}$ is the bandwidth of energy spectrum.

To examine the effectiveness of the selection strategy, as shown in Figs. S12**a**, **b**, and **c**, we plot the overlaps between five randomly selected initial states and all eigenstates for $4 \times 4$ 2D SSH model for different disorders. We find that the middle eigenstates have much larger overlaps with our initial states than the marginal ones. Furthermore, as the disorder strength increases, the distribution of overlap over energy eigenstates becomes narrower. Figs. S12**d**, **e**, and **f** display the overlap for the scarred initial state $|\mathbf{s}_0^S\rangle$. For $V = 0$, it shows a multi-peak behavior (Fig. S12**d**). In the presence of large disorder $V \approx 16J_0$, all these peaks shrink to a sharp one (Fig. S12**f**). Its position deviates a little from the center due to the change of total energy caused by disorders.

## 10. DERIVATION OF ERGODIC WAVE PACKET

Our model is a hard-core Bose-Hubbard model, and the total particle number is conserved during the time evolution. In the half-filling condition, $\Pi(d)$ vanishes for the odd Hamming distance $D(\mathbf{s}, \mathbf{s}_0)$, since a photon hopping from one site to another sit leads to a change of two for $D(\mathbf{s}, \mathbf{s}_0)$. Thus, values of Hamming distance are a set of even integers as $d = 0, 2, 4, \cdots, L$ for our system.

For the ideal ergodic wavefunction, its overlap with each Fock-space site is the same. Thus, we have a hypergeometric-like distribution as

$$\Pi^{\rm Erg.}(d) = \frac{C_{L/2}^{d/2} C_{L/2}^{L/2-d/2}}{C_L^{L/2}}. \tag{S10}$$

Then, the displacement is given by

$$\overline{d} = \sum_d \Pi(d) \cdot d = \frac{1}{2} \sum_d \frac{C_{L/2}^{d/2} C_{L/2}^{L/2-d/2}}{C_{L-1}^{L/2-1}} \cdot d = \frac{L}{2}. \tag{S11}$$

Variance is defined as $\Delta d^2 = \overline{d^2} - \overline{d}^2$ with $\overline{d^2} = \overline{d(d-1)} +$

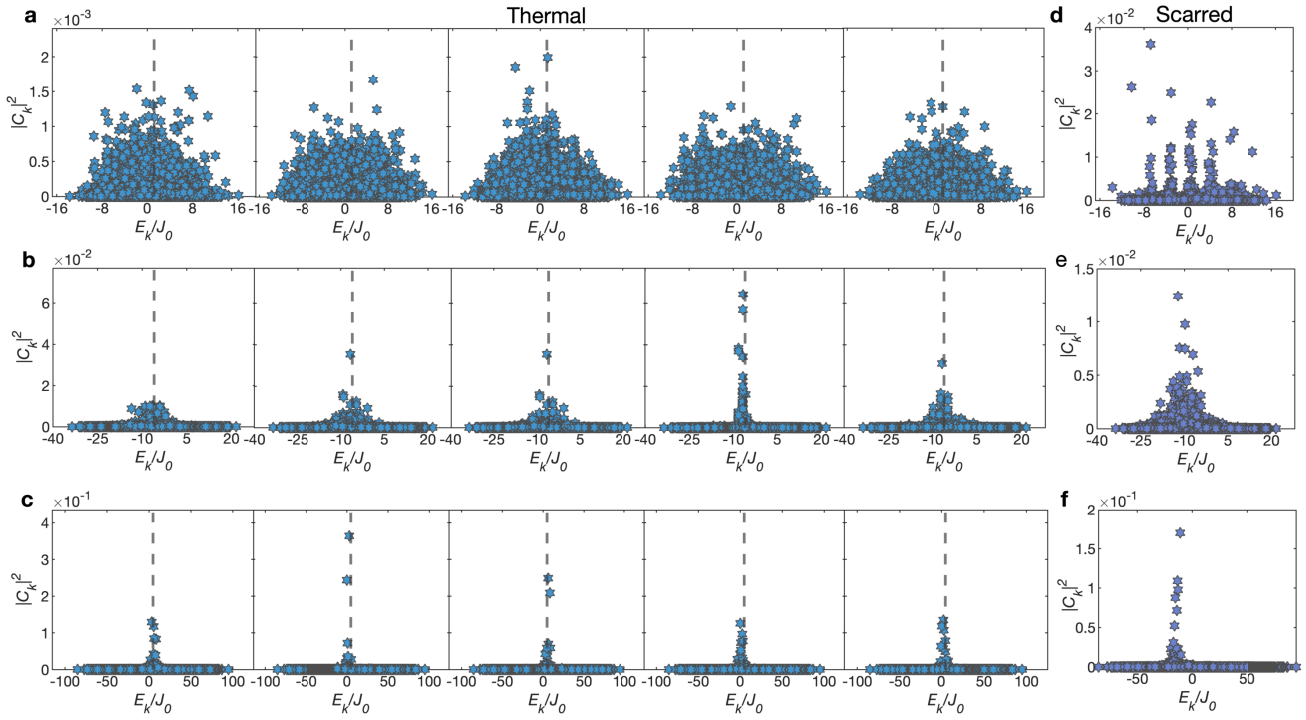


FIG. S12. **Overlaps between initial states and eigenstates.** Panels **a**, **b**, and **c** show the overlaps $|C_k|^2 = |\langle \mathbf{s}_0|E_k\rangle|^2$ between five randomly selected initial states and eigenstates in $4\times4$ 2D SSH system ($J_o/2\pi = 2J_e/2\pi = -6$ MHz, $g_x/2\pi = 0.9$ MHz), with disorder strength $V = 0$, $V \approx 6J_0$, and $V \approx 16J_0$, respectively. Each state is randomly selected in the energy window $[E_{\rm mid} - \Delta E/100, E_{\rm mid} + \Delta E/100]$. The gray dashed line indicates the center of the energy spectrum. Panel **d** shows the overlap spectrum for the scarred state $|\mathbf{s}_0^S\rangle$ at $V = 0$, where multi-tower feature with higher overlap on some special eigenstates appears. Panels **e** and **f** are the similar results at $V \approx 6J_0$ and $V \approx 16J_0$, respectively. With the growing disorder strength, the multi-tower feature fades and keeps only one peak near its total energy.

$\overline{d}$. We have

$$\begin{aligned}\overline{d(d-1)} &= \sum_d \frac{C_{L/2}^{d/2} C_{L/2}^{L/2-d/2}}{C_L^{L/2}} d(d-1) \\ &= \frac{L}{4}\frac{L^2-2L+2}{L-1},\end{aligned}$$

thus,

$$\Delta d^2 = \overline{d(d-1)} + \overline{d} - \overline{d}^2 = \frac{L^2}{4(L-1)}.$$

In conclusion, for the ergodic wave packet, normalized displacement $\mathrm{x}^{\rm Erg.} = \overline{d}/L = 0.5$ and normalized width $\Delta\mathrm{x}^{\rm Erg.} = \frac{\sqrt{L-1}}{L}\sqrt{\Delta d^2} = 0.5$. Moreover, the system fluctuation $\sigma$, as it has been introduced in the main text, would be $\sigma = \frac{\sqrt{L-1}}{L}\sqrt{\sum_d d^2\Pi(d) - \langle \mathrm{x}\rangle^2} = 0.5$.

## 11. NUMERICAL SIMULATION OF $4\times4$ LATTICE

In this section, we numerically compare our Fock-space wave packet approach with the conventional observables, such as level statistics, inverse participation ratio, and entanglement entropy on a $4\times4$ 2D SSH lattice.

In the random matrix theory, the statistics of level spacing $s_i$ between two nearest eigenenergies $E_i$ and $E_{i+1}$ is a standard way to differentiate ergodic and nonergodic systems. For a quantum chaotic system, its distribution shows a Gauss orthogonal ensemble (GOE) type, $P_{\rm GOE} = \frac{\pi}{2}s\mathrm{e}^{-(\pi/4)s^2}$ [9], whereas a Poisson distribution, $P_{\rm Poisson}(s) = e^{-s}$, is expected when a quantum many-body system is localized. Different kinds of level spacing statistics can be characterized by the level spacing ratio $r_i = \min(s_{i+1}/s_i, s_i/s_{i+1})$. The mean value $\langle r\rangle$ at central energy spectrum regime, levels off $(2\ln2-1) \approx 0.386$ or $(4-2\sqrt{3}) \approx 0.536$ for an integrable or a GOE distribution, respectively [10]. Figure S13**a** shows that $\langle r\rangle$ is equal to about 0.53 for weak disorder regime ($V < 4J_0$) and drops to the Poisson distribution value 0.39 for the strong disorder regime near $V \approx 16J_0$. For comparison, the disorder-averaged normalized displacement $\langle \mathrm{x}\rangle$ is also plotted in Fig. S13**a**.

In Fock space, the multifractal analysis of inverse participation ratio (IPR) is a popular way to characterize MBL transition. Here, we use 2-moment generalized frac-

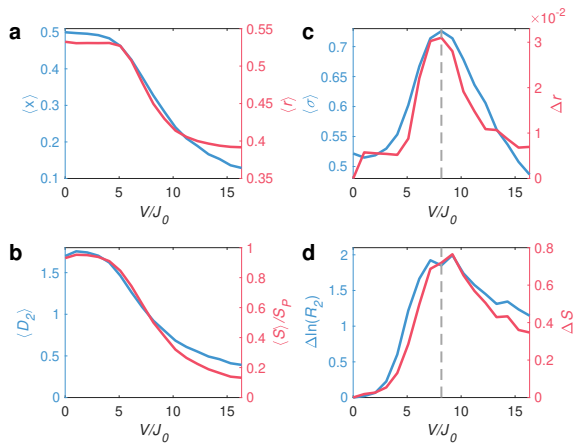


FIG. S13. **Numerical simulation of MBL indicators with eigenstate properties.** **a**. Disorder-averaged normalized displacement $\langle \mathrm{x} \rangle$ (blue) and level spacing ratios $\langle r \rangle$ (red) as a function of disorder strength $V$. **b**. Disorder-averaged 2-moment generalized fractal dimension $\langle D_2 \rangle$ (blue) and rescaled bipartite EE $\langle S \rangle / S_P$ (red) as a function of disorder strength $V$. **c**, Fluctuation of wave packets $\langle \sigma \rangle$ (blue) and standard deviation of level spacing ratios $\Delta r$ (red) as a function of disorder strength $V$. **d**, Standard deviation of bipartite EE $\Delta S$ (red) and standard deviation of 2-moment IPR $\Delta \ln(\mathrm{R}_2)$ (blue) as a function of disorder strength $V$. The gray dashed lines in **c** and **d** indicate the critical point of the finite-size MBL transition for $4 \times 4$ lattice. The model for numerics is the $4 \times 4$ SSH lattice with $J_o/2\pi = 2J_e/2\pi = -6$ MHz and $g_x/2\pi = 0.9$ MHz. For each $V$, we randomly choose $k = 800$ disorder realizations and randomly select ten eigenstates in the middle energy spectrum for each of them.

tal dimension, which is given by [11]

$$D_2 = -\ln R_2 / \ln \mathcal{N}, \tag{S12}$$

where the inverse participation ratio $R_2 = \mathrm{IPR}_2 = \sum_\alpha |\psi_\alpha|^4$. $\{|\alpha\rangle\}$ is a set of orthonormal basis of an $\mathcal{N}$-dimension Hilbert space and $|\psi\rangle = \sum_\alpha \psi_\alpha |\alpha\rangle$. As shown in Fig. S13**b**, $D_2$ decays monotonically as disorder strength grows and the bipartite EE also shows similar behaviors.

To extract the critical disorder, the fluctuations, such as $\langle \sigma \rangle$, $\Delta r$, $\Delta \ln(R_2)$, and $\Delta S$ are displayed in Figs. S13**c** or **d**. In spite of the slight difference, all of them indicate almost the same critical disorder near $\sim 8J_0$.

## 12. ERROR MITIGATION

To mitigate state preparation and measurement (SPAM) errors, and qubit energy relaxation ($T_1$) errors, our error mitigation scheme includes readout correction and post-selection in the data processing [5, 12]. Here, we illustrate detailed information about them.

As shown in Table S1, we list readout fidelities $\{F_{0,(m,n)}, F_{1,(m,n)}\}$ for each qubit. Thus, the readout correction matrix for qubit $Q_{(m,n)}$ is given by

$$S_{(m,n)} = \begin{pmatrix} F_{0,(m,n)} & 1 - F_{1,(m,n)} \\ 1 - F_{0,(m,n)} & F_{1,(m,n)} \end{pmatrix}. \tag{S13}$$

Then, the corrected probability vector for the system is given by $\vec{P}_{\mathrm{corr}} = \bigotimes_{(m,n)} S^{-1}_{(m,n)} \cdot \vec{P}$, where $\vec{P}$ is the raw probability vector. Moreover, since our model conserves the total photon number during the time dynamics, we could mitigate T1 induced photon leakage errors by only keeping the photon-number-conserved subspace of $P_{\mathrm{corr}}$.

Thanks to the coherent oscillating dynamics of the scarred state, we can clearly see effects of our error mitigation scheme step by step. In Fig. S14, we compare the numerical results with experimental results with and without using the error mitigation scheme. Obviously, both readout correction and post-selection remarkably improve the quality of experimental data.

In addition, we emphasize that the observation of critical behavior of MBL transition with $\Delta \mathrm{x}$ and $\sigma$ are quite robust to SPAM errors and energy relaxation errors. It is a crucial point for a scalable protocol, since the readout correction scheme above is inaccessible for large systems. In Fig. S15, we compare the raw data and the corrected data. The differences mainly appear in the strong disorder regime, while the critical regime and the critical point almost do not change .

## 13. EFFECT OF DECOHERENCE

Decoherence is inevitable for current experimental platforms, which is caused by the small couplings between the system and the surrounding environments. Decoherence has two effects on qubits: energy relaxation and dephasing. The energy relaxation is characterized by the energy relaxation time $T_1$, as listed in Table. S1. $T_1$ ($\sim 120$ $\mu$s) in our device is far larger than the maximum experimental time (1 $\mu$s) and we use the post-selection method to mitigate its effect (see Sec. 12).

The effect of dephasing is much more complicated, especially for the interacting many-body system with all qubits actively coupled. Here, we demonstrate that the true dephasing times describing the coupled qubits are much longer than that measured by Ramsey experiments ($T_2^*$), whose timescales ($\sim 20$ $\mu$s) are similar to spin echo dephasing times $T_2^{SE}$.

We choose nearest-neighbor qubit pairs, i.e., $Q_{(1,1)}$-$Q_{(1,2)}$, $Q_{(1,2)}$-$Q_{(1,3)}$, and $Q_{(2,3)}$-$Q_{(2,4)}$ to measure two-qubit resonant swap dynamics for each pair at 4.57 GHz. The coupling strength is set to $J_{\mathrm{NN}}/2\pi \approx -6$ MHz or $-3$ MHz. The experimental results of swap dynamics are shown in Fig. S16. We fit the probability $P_{10}$ with the following formula [5]

$$P_{10}(t) = \frac{1}{2}\cos(2J_{\mathrm{NN}}t)e^{-\frac{t}{\bar{T}_1}-\frac{t}{T_\phi}} + \frac{1}{2}e^{-\frac{t}{\bar{T}_1}}, \tag{S14}$$

where $\bar{T}_1 = 2T_{1,m}T_{1,m+1}/(T_{1,m} + T_{1,m+1})$ is the average energy relaxation lifetime for the qubit pair, and $T_\phi$ is the

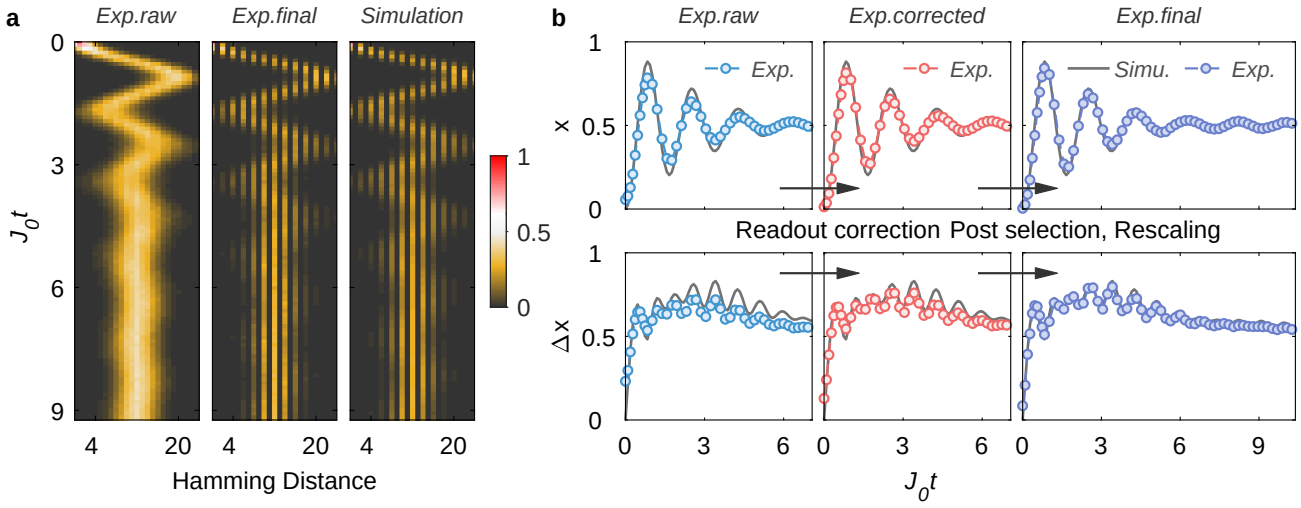


FIG. S14. **Effects of error mitigation. a**. Experimentally measured wave packet dynamics are shown in the left panel for the results extracted with raw data, and in the middle panel for the results using error mitigation. For comparison, the numerical results are shown in the right panel, which almost perfectly match the error-mitigated experimental results. **b.** Effects of readout correction and post-selection for normalized displacement x and normalized displacement Δx. The results with readout correction are shown in the middle column, based on which the post-selection is further applied and the results are shown in the right column. The experimental and numerical data are obtained on the half-filling $4 \times 6$ SSH model in the main text.

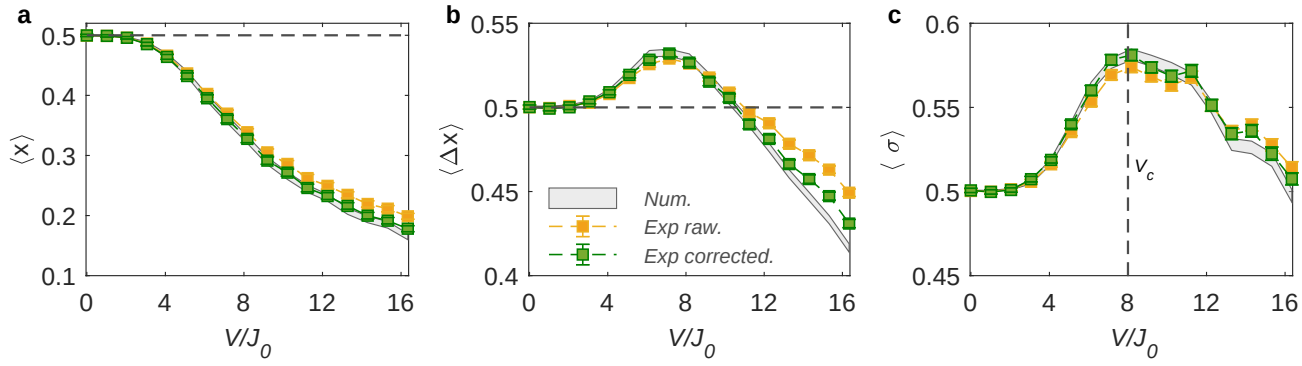


FIG. S15. **Robustness to errors. a**, **b**, and **c** are long-time ($t = 1000$ ns) disorder-averaged normalized displacement $\langle x \rangle$, normalized width $\langle \Delta x \rangle$, and system fluctuation $\langle \sigma \rangle$ as a function of disorder strength $V$, respectively. Green squares are experimental data with error mitigation while yellow squares denote the raw data. The light gray areas represent numerical results. Despite some deviations, we can still clearly identify the critical regime and critical point. For each $V$, we randomly choose $k = 400$ disorder realizations.

effective dephasing time during the interaction. In this way, the effective dephasing times for qubit pairs $Q_{(1,2)}$-$Q_{(1,3)}$, $Q_{(1,2)}$-$Q_{(1,3)}$ and $Q_{(2,3)}$-$Q_{(2,4)}$, are estimated with values of 25 $\mu$s, 24 $\mu$s, and 14 $\mu$s (see Fig. S16), respectively, which are one order of magnitude larger than the maximum experimental time (1 $\mu$s). Thus, it is reasonable to approximately treat our system as a closed quantum system within the experimental timescale.

## 14. FINITE-TIME EFFECT

In general, properties of eigenstates are the starting point for studying the MBL phase transition [13, 14]. However, current experimental techniques only allow us to observe out-of-equilibrium quench dynamics within a finite timescale. The evolution time needs to be large enough in order to observe quantum thermalization and its breakdown. Therefore, it is necessary to demonstrate that the evolution time in our experiment (1000 ns) is sufficient to imply the nature of the system. We numerically investigate such an effect by varying the evolution time and compare the results in infinite-time limit ob-

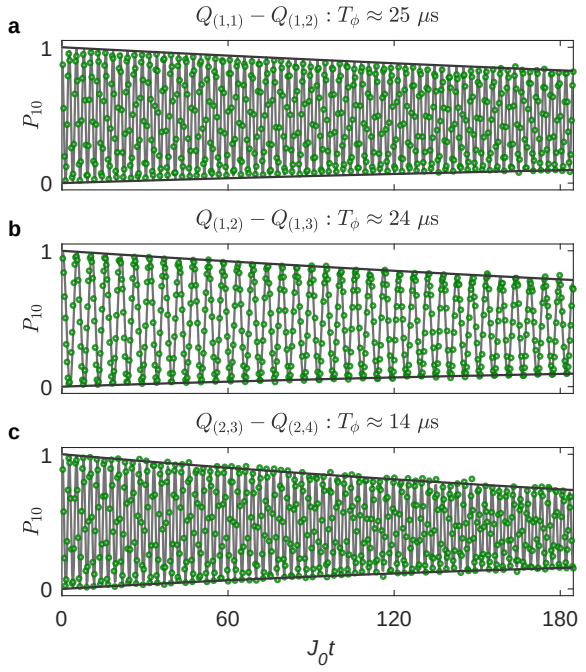


FIG. S16. **Effective dephasing time $T_\phi$ for coupled qubit pairs.** $P_{10}$ dynamics of qubit pairs are shown in **a** for $Q_{(1,1)}$-$Q_{(1,2)}$, **b** for $Q_{(1,2)}$-$Q_{(1,3)}$, and **c** for $Q_{(2,3)}$-$Q_{(2,4)}$. Green circles denote the experimental data and gray lines are the corresponding fitting data using Eq. S14, which give the effective dephasing time about 25 $\mu$s, 24 $\mu$s, and 14 $\mu$s for them.

tained by eigenstates.

The relation between the eigenstates and time evolution of a quantum state is given by ($\hbar = 1$)

$$|\psi(t)\rangle = e^{-i\hat{H}t}|\psi(0)\rangle = \sum_k C_k e^{-iE_k t}|E_k\rangle, \tag{S15}$$

where $|\psi(t)\rangle$ is the time-dependent wavefunction. Therefore, an infinite-time operator $\langle\hat{O}\rangle_{t\to\infty}$ can be written as

$$\begin{aligned}\langle\hat{O}\rangle_{t\to\infty} &\equiv \lim_{t\to\infty}\frac{1}{t}\int_0^t \langle\psi(\tau)|\hat{O}|\psi(\tau)\rangle d\tau \\ &\approx \sum_k |C_k|^2\langle E_k|\hat{O}|E_k\rangle.\end{aligned} \tag{S16}$$

According to Eq. S16, we can obtain the radial probability distribution at infinite time as

$$\begin{aligned}\Pi(d)_{t\to\infty} &= \lim_{t\to\infty}\sum_{\mathbf{s}\in\{D(\mathbf{s},\mathbf{s}_0)=d\}} \langle\psi(t)|\mathbf{s}\rangle\langle\mathbf{s}|\psi(t)\rangle \\ &= \sum_k |C_k|^2 \sum_{\mathbf{s}\in\{D(\mathbf{s},\mathbf{s}_0)=d\}} |\langle E_k|\mathbf{s}\rangle|^2,\end{aligned} \tag{S17}$$

where $D(\mathbf{s},\mathbf{s}_0)$ is the Hamming distance between state $|\mathbf{s}\rangle$ and $|\mathbf{s_0}\rangle$. Once we get the $\Pi(d)_{t\to\infty}$, we can calculate the wave packet displacement, width and fluctuation.

The numerical results for disorder-averaged $\langle$x$\rangle$, $\langle\Delta$x$\rangle$, and $\langle\sigma\rangle$ at different times are shown in Fig. S17, we find that the results at timescale in our experiment ($t = 1000$ ns) have similar transition behaviors with eigenstates. We note that despite a higher peak of $\langle\Delta$x$\rangle$ for eigenstate results, the peak position for identifying critical transition point is almost the same for both eigenstate results and finite-time results.


[1] F. Yan, P. Krantz, Y. Sung, M. Kjaergaard, D. L. Campbell, T. P. Orlando, S. Gustavsson, and W. D. Oliver, Tunable coupling scheme for implementing high-fidelity two-qubit gates, Phys. Rev. Applied **10**, 054062 (2018).

[2] X. Zhang, W. Jiang, J. Deng, K. Wang, J. Chen, P. Zhang, W. Ren, H. Dong, S. Xu, Y. Gao, F. Jin, X. Zhu, Q. Guo, H. Li, C. Song, A. V. Gorshkov, T. Iadecola, F. Liu, Z.-X. Gong, Z. Wang, D.-L. Deng, and H. Wang, Digital quantum simulation of Floquet symmetry-protected topological phases, Nature **607**, 468 (2022).

[3] S. Bravyi, D. P. DiVincenzo, and D. Loss, Schrieffer–Wolff transformation for quantum many-body systems, Annals of Physics **326**, 2793 (2011).

[4] P. Zhang, H. Dong, Y. Gao, L. Zhao, J. Hao, Q. Guo, J. Chen, J. Deng, B. Liu, W. Ren, Y. Yao, X. Zhang, S. Xu, K. Wang, F. Jin, X. Zhu, H. Li, C. Song, Z. Wang, F. Liu, Z. Papić, L. Ying, H. Wang, and Y.-C. Lai, Many-body hilbert space scarring on a superconducting processor, Nature Physics , 1 (2022).

[5] Q. Guo, C. Cheng, Z.-H. Sun, Z. Song, H. Li, Z. Wang, W. Ren, H. Dong, D. Zheng, Y.-R. Zhang, R. Mondaini, H. Fan, and H. Wang, Observation of energy-resolved many-body localization, Nature Physics **17**, 234 (2021).

[6] C. Turner, A. Michailidis, D. Abanin, M. Serbyn, and Z. Papic, Weak ergodicity breaking from quantum many-body scars, Nature Physics **14** (2018).

[7] R. Hamazaki and M. Ueda, Atypicality of most few-body observables, Physical Review Letters **120**, 10.1103/physrevlett.120.080603 (2018).

[8] D. J. Luitz, N. Laflorencie, and F. Alet, Many-body localization edge in the random-field Heisenberg chain, Phys. Rev. B **91**, 081103 (2015).

[9] T. Guhr, A. Müller–Groeling, and H. A. Weidenmüller, Random-matrix theories in quantum physics: common concepts, Physics Reports **299**, 189 (1998).

[10] F. M. Izrailev, Simple models of quantum chaos: Spectrum and eigenfunctions, Physics Reports **196**, 299 (1990).

[11] F. Evers and A. D. Mirlin, Anderson transitions, Reviews of Modern Physics **80**, 1355 (2008).

[12] G. A. Quantum and collaborators, Observation of separated dynamics of charge and spin in the Fermi-Hubbard model, arXiv:2010.07965 (2020).

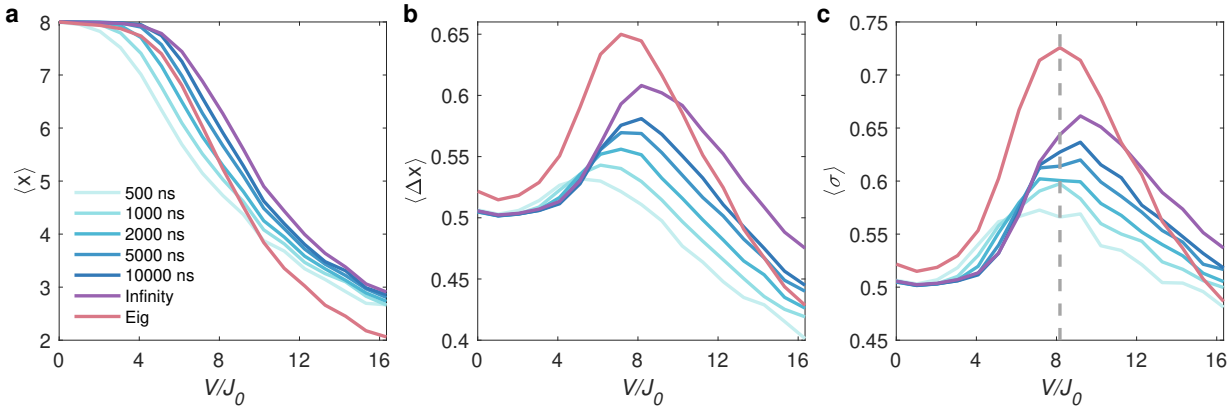


FIG. S17. **Finite-time effects.** Numerical results at different timescales as well as eigenstate results are shown in panel **a** for normalized displacement $\langle \mathrm{x} \rangle$, panel **b** for normalized width $\langle \Delta \mathrm{x} \rangle$, and panel **c** for system fluctuation $\langle \sigma \rangle$. All of them are averaged over $k = 800$ disorder realizations. Red curves represent the eigenstate results and the purple lines represent the results at infinite-time limit. The cyan-blue gradient curves show the time evolution of 500 ns, 1000 ns, 2000 ns, 5000 ns, and 10000 ns. In panel **c**, the dashed line labels the critical point estimated by eigenstate results. All the data are obtained on $4 \times 4$ SSH model with $J_\mathrm{o}/2\pi = 2J_\mathrm{e}/2\pi = -6$ MHz and $g_\mathrm{x}/2\pi = 0.9$ MHz.

[13] M. Rigol, V. Dunjko, and M. Olshanii, Thermalization and its mechanism for generic isolated quantum systems, Nature (London) **452**, 854 (2008).
[14] V. Khemani, S. P. Lim, D. N. Sheng, and D. A. Huse, Critical properties of the many-body localization transition, Phys. Rev. X **7**, 021013 (2017).